







| | |
|-------------|--|
| Title | The Impact of Progenitor Mass Loss on the Dynamical and Spectral Evolution of Supernova Remnants |
| Author(s) | Patnaude, Daniel J.; Lee, Shiu-Hang; Slane, Patrick O.; Badenes, Carles; Nagataki, Shigehiro; Ellison, Donald C.; Milisavljevic, Dan |
| Citation | The Astrophysical Journal (2017), 849(2) |
| Issue Date | 2017-11-10 |
| URL | http://hdl.handle.net/2433/252783 |
| Right | © 2017. The American Astronomical Society. All rights reserved. |
| Type | Journal Article |
| Textversion | publisher |



The Impact of Progenitor Mass Loss on the Dynamical and Spectral Evolution of Supernova Remnants

Daniel J. Patnaude¹ , Shiu-Hang Lee², Patrick O. Slane¹ , Carles Badenes^{3,4} , Shigehiro Nagataki⁵ ,
Donald C. Ellison⁶ , and Dan Milisavljevic^{1,7} 

¹ Smithsonian Astrophysical Observatory, Cambridge, MA 02138, USA; dpatnaude@cfa.harvard.edu, herman@kusastro.kyoto-u.ac.jp

² Kyoto University, Department of Astronomy, Oiwake-cho, Kitashirakawa, Sakyo-ku, Kyoto 606-8502, Japan

³ Department of Physics and Astronomy and Pittsburgh Particle Physics, Astrophysics and Cosmology Center (PITT PACC), University of Pittsburgh, 3941 O'Hara Street, Pittsburgh, PA 15260, USA

⁴ Institut de Ciències del Cosmos, Universitat de Barcelona (ICCUB), Martí i Franques 1, Barcelona, E-08028, Spain

⁵ RIKEN, Astrophysical Big Bang Laboratory & Interdisciplinary Theoretical and Mathematical Science Program, 2-1 Hirosawa, Wako, Saitama 351-0198, Japan

⁶ Department of Physics, North Carolina State University, Raleigh, NC 27695-8202, USA

⁷ Purdue University, Department of Physics and Astronomy, 525 Northwestern Avenue, West Lafayette, IN 47907, USA

Received 2017 August 16; revised 2017 September 22; accepted 2017 October 3; published 2017 November 7

Abstract

There is now substantial evidence that the progenitors of some core-collapse supernovae undergo enhanced or extreme mass loss prior to explosion. The imprint of this mass loss is observed in the spectra and dynamics of the expanding blast wave on timescales of days to years after core collapse, and the effects on the spectral and dynamical evolution may linger long after the supernova has evolved into the remnant stage. In this paper, we present, for the first time, largely self-consistent end-to-end simulations for the evolution of a massive star from the pre-main sequence, up to and through core collapse, and into the remnant phase. We present three models and compare and contrast how the progenitor mass-loss history impacts the dynamics and spectral evolution of the supernovae and supernova remnants. We study a model that only includes steady mass loss, a model with enhanced mass loss over a period of ~ 5000 yr prior to core collapse, and a model with extreme mass loss over a period of ~ 500 yr prior to core collapse. The models are not meant to address any particular supernova or supernova remnant, but rather to highlight the important role that the progenitor evolution plays in the observable qualities of supernovae and supernova remnants. Through comparisons of these three different progenitor evolution scenarios, we find that the mass loss in late stages (during and after core carbon burning) can have a profound impact on the dynamics and spectral evolution of the supernova remnant centuries after core collapse.

Key words: circumstellar matter – ISM: supernova remnants – nuclear reactions, nucleosynthesis, abundances – stars: mass-loss – supernovae: general – X-rays: general

1. Introduction

When interpreting the remnants of core-collapse supernovae (CCSNe), assumptions regarding the isotropy of the progenitor mass loss are frequently made. Often times, it is assumed that the mass loss remained steady up to core collapse (see Chevalier 2005). However, the endpoint in massive star evolution is poorly understood. In particular, violent and episodic mass loss is now observed in the progenitors of some CCSNe, most notably in SN 2009ip ($\dot{M} \sim 0.1 M_{\odot} \text{ yr}^{-1}$; Fraser et al. 2013; Mauerhan et al. 2013; Pastorello et al. 2013; Margutti et al. 2014; Smith et al. 2014), though substantial evidence exists for extreme mass loss in other SNe IIn (Ofek et al. 2013, 2014; Elias-Rosa et al. 2016; Smith et al. 2017). More exotic mass loss is ascribed to SNe Ibn (e.g., SN 2006jc; Pastorello et al. 2008) and SNe Ib/c that transition to Type IIn after some time, including SN 2001em (Chugai & Chevalier 2006) and SN 2014C (Milisavljevic et al. 2015; Margutti et al. 2017). Even in “normal” SNe I Ib/II and SNe IIP, evidence for enhanced mass loss (relative to rates observed in red supergiants [RSGs]; Smith 2014) is observed (e.g., Milisavljevic et al. 2013; Maeda et al. 2015; Chakraborti et al. 2016; Kamble et al. 2016; Morozova et al. 2017).

The origin of the extreme mass loss remains a mystery, but several theories have been suggested. For instance, the onset of core carbon and oxygen burning can lead to stellar cores that are super-Eddington. Some of this energy could be tapped by as of yet poorly understood processes in the core (Quataert &

Shiode 2012; Shiode & Quataert 2014). If the progenitor is sufficiently compact, convectively driven waves could rise to the surface and unbind envelope material, depositing it into the circumstellar environment. Similarly, nuclear shell burning could lead to unstable flows near the surface, possibly also ejecting material on timescales that are short relative to the life of the progenitor (Smith & Arnett 2014).

On longer timescales, stable mass transfer or common envelope evolution could remove material from the surface of the progenitor (de Mink et al. 2013). In the case of a common envelope binary system, the H-rich envelope could be removed prior to core collapse (e.g., Podsiadlowski et al. 1992). Whatever the mechanism, evidence for enhanced mass loss prior to core collapse is observed, either directly through massive eruptions by so-called SN impostors or through the interaction of the blast wave with a circumstellar shell of ejected material, as in some SNe IIn or even more typical SNe IIP/II/IIb.

As illustrated in Figure 1, while SNe sample the stages of evolution much closer to core collapse, supernova remnants (SNRs) typically probe stellar evolution on much longer timescales (see Patnaude & Badenes 2017). This is because the timescale for the evolution of the circumstellar environment is set by the outflow speed of the wind, while the evolutionary timescale for the SNR is determined by the blast-wave velocity. For example, a $10,000 \text{ km s}^{-1}$ shock that expands into a 10 km s^{-1} wind samples 1000 yr of stellar evolution for every

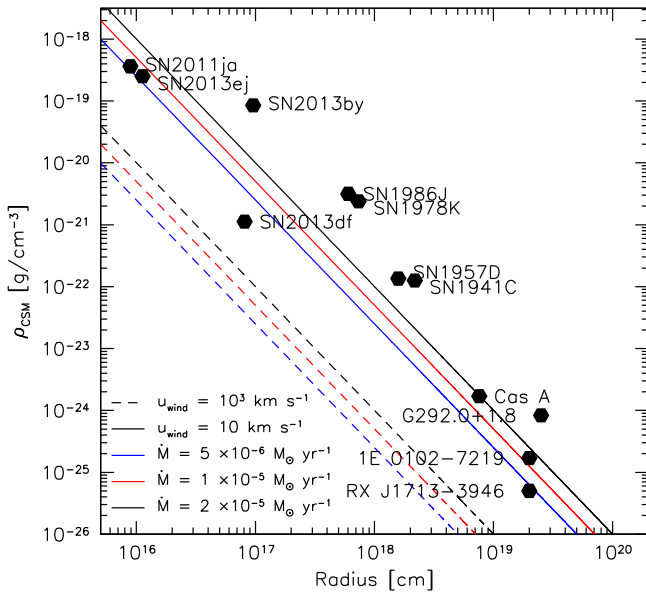


Figure 1. Comparison of SNe and SNR radii with those predicted via various mass-loss rates and outflow speeds. The SN/SNR radii can be related back to the time before core collapse, if assumptions about the shock speed and wind speed are made, since $t_{\text{shock}} = v_{\text{wind}} \times t_{\text{wind}} / v_{\text{shock}}$. For SNe, radii are derived from the X-ray emission, assuming a wind speed of 10 km s^{-1} (Immler & Lewin 2003). Data are from Ross & Dwarkadas (2017), Long et al. (2012), and Soria & Perna (2008). Data for SNRs are from Patnaude et al. (2009), Lee et al. (2010), and Ellison et al. (2012).

year of blast-wave evolution—a 100 yr old SNR has probed a significant portion of the RSG phase of a massive star’s life. This would imply that SNR shocks are not effective probes of the latter stages of stellar evolution, since they interact with material lost primarily during core helium burning.

However, while the characteristic timescale for SNR evolution is a few thousand years and is dependent on the explosion energetics, ejecta mass, and circumstellar density (Truelove & McKee 1999), the timescale for ions and electrons to recombine in a partially ionized plasma is $\sim 10^{12}/n_e \text{ s}$, where n_e is the number density of electrons. The circumstellar density around a massive star is generally thought to decrease with increasing radius owing to flux conservation in the stellar wind (Dwarkadas 2005, 2007; Dwarkadas & Gruszko 2012). Hence, as the SN shock expands into the wind, the density of shocked material decreases, so that n_e is a decreasing function of SN age. This suggests that the recombination timescale in the plasma increases with increasing remnant age, and any circumstellar interaction that occurs early in the remnant evolution could be detectable at later remnant ages.

Oftentimes, the X-ray spectrum from shocked circumstellar material is modeled as a blast wave interacting with a progenitor wind where the density $\rho_{\text{CSM}} \propto r^{-2}$. However, in Patnaude et al. (2015), we demonstrated that many SNRs do not always show X-ray emission that is consistent with the interaction between the ejecta and a power-law wind. We argued that enhanced mass loss prior to core collapse could greatly increase the X-ray luminosity without strongly affecting the blast-wave radius. This is because the X-ray emission scales like the density squared, while the blast-wave radius is only a weak function of the ambient medium.

In this paper, we extend Patnaude et al. (2015) by following the end-to-end evolution of a massive star, from the pre-main

sequence through the remnant phase. We accomplish this by using the MESA stellar evolution code to construct three different massive progenitor scenarios: one where the progenitor loses very little mass to a standard power-law wind, one where the star is stripped of some of its envelope during core carbon burning, and one where the H envelope is almost entirely removed during core oxygen burning. We use the mass-loss history of the progenitor to construct its circumstellar environment. Using a version of the SuperNova Explosion Code (SNEC)⁸ modified to follow the explosive nucleosynthesis that occurs during core collapse, we explore these progenitors, computing the velocity and density fields of the ejecta, as well as its composition. We follow the evolution of these models to ages of 400 yr with our ChN code, simulating circumstellar medium (CSM) properties appropriate for each mass-loss scenario. In Section 2, we describe in detail each model component and address the uncertainties associated with each model. In Section 3, we present and discuss our models. We present our conclusions in Section 4.

2. End-to-end Models

In this section, we discuss the chain of models we use to simulate the stellar evolution up to, through, and beyond core collapse. In each subsection, we discuss the models used for each evolutionary stage. In the last subsection we discuss the uncertainties in our approach. We stress that no model is tailored to address any particular SN or remnant and that we are presenting a parameterized framework with which we can study more specific scenarios in the future.

2.1. Stellar Evolution Models

Models for $15 M_{\odot}$ progenitors are evolved using Modules for Experiments in Stellar Astrophysics (hereafter MESA, version 8845; Paxton et al. 2011, 2013, 2015).⁹ All models are initialized at solar metallicity ($Z = 0.02$). We evolve three models, without rotation, but we employ the “Dutch” wind scheme (Nieuwenhuijzen & de Jager 1990; Nugis & Lamers 2000; Vink et al. 2001; Glebbeek et al. 2009) with an efficiency $\eta = 0.8$. Each model is evolved from the pre-MS through core collapse, which we define as the time when the infall velocity at any location is $\geq 1000 \text{ km s}^{-1}$. For each model, we use MESA inlists made available from Farmer et al. (2016). We follow their scheme for specifying the mass and temporal evolution of the models during burning phases leading up to core collapse.

We make use of the `aprox21` nuclear burning network. This is chosen (1) for speed and efficiency and (2) to match the burning network we have added to our SN models (Section 2.2). While Farmer et al. (2016) concluded that the final electron fraction and mass locations of the primary nuclear burning shells can vary by $\approx 30\%$ based on the choice of nuclear burning network, and that a minimum of 127 isotopes are needed in order to gain convergence in these values at levels of 10% or better, we note that we are interested in the bulk qualities of X-ray spectra from astrophysically abundant elements (O, Si, S, Fe, etc.). Additionally, since we are comparing the synthesized X-ray spectra among models and not making any comparisons of final elemental yields to observations, we feel that our choice of nuclear burning

⁸ <http://stellarcollapse.org/SNEC>

⁹ www.mesa.sourceforge.net

Table 1
MESA Initial and Final Model Parameters

| Model | M_{Final} | M_C | M_O (M_{\odot}) | M_{Si} | M_{Fe} | R ($\log_{10} R/R_{\odot}$) | \dot{M}^a ($M_{\odot} \text{ yr}^{-1}$) | $t_{\text{mass-loss}}$ (yr) |
|--------|--------------------|-------|--------------------------|-----------------|-----------------|------------------------------------|--|--------------------------------|
| m15Iso | 13.3 | 2.56 | 2.48 | 1.70 | 1.53 | 2.99 | 5×10^{-6} | 11.1×10^7 |
| m15C | 10.0 | 2.56 | 2.49 | 1.68 | 1.51 | 3.03 | 2×10^{-4} | 5000 |
| m15O | 5.7 | 2.56 | 2.46 | 1.69 | 1.53 | 2.93 | 0.1 | 50 |

Note.

^a Mass-loss rates are given for the time period of interest. For the isotropic case, the average mass-loss rate of $5 \times 10^{-6} M_{\odot} \text{ yr}^{-1}$ is used.

network satisfies our requirement for speed and efficiency while also capturing the spirit of the necessary physics.

We specify three models. Model m15Iso uses the Dutch wind models up to the onset of core collapse. The average mass-loss rate over the lifetime of the star is $\sim 5 \times 10^{-6} M_{\odot} \text{ yr}^{-1}$. Model m15C includes enhanced mass loss during core carbon burning, at a constant rate of $2 \times 10^{-4} M_{\odot} \text{ yr}^{-1}$, resulting in ~ 2 additional solar masses of material deposited into the circumstellar environment. When core oxygen burning begins, we revert to mass-loss rates from the Dutch scheme. Model m15O follows isotropic mass loss up to core oxygen burning, at which point we employ extreme mass loss. In this case, the mass loss is held fixed at $0.1 M_{\odot} \text{ yr}^{-1}$. We include this extreme mass loss until the formation of the silicon core. During this phase, the progenitor loses $\sim 6 M_{\odot}$ of material. At the onset of core collapse, our models have final masses of $\sim 13, 10,$ and $6 M_{\odot}$.

We stress that the enhanced and extreme mass-loss models are not meant to represent any physical processes associated with late-stage stellar evolution. While there is growing evidence for enhanced mass loss in SN progenitors prior to core collapse, from timescales of roughly a few thousand years down to timescales of a few years, the mechanism for this mass loss remains poorly understood and could result from hydrodynamic instabilities and turbulence in the outer layers of the star (Smith & Arnett 2014), wave-driven mass loss due to energy extraction from the super-Eddington core (Quataert & Shiode 2012; Shiode & Quataert 2014), or pulsational-driven superwinds (Yoon & Cantiello 2010), among other possibilities. In this study, we are aiming to deposit the mass in the CSM at a position that is self-consistent with the timing of the mass loss epoch.

While the exact mass-loss mechanism will undoubtedly alter the final evolution of the progenitor, we look to understand how the mass loss affects the evolution of the SNR, independent of how it arose. In Table 1 we present the initial and final parameters for each model, while in Figure 2 we plot the density and temperature of the progenitors for each model at the onset of core collapse. Beyond the large differences in final mass, brought about by the choice of fiducial mass loss, there are not large differences in the final parameters of the progenitors, with the most notable differences being in the final progenitor radii. As seen in Figure 2, the thermodynamic profiles of the progenitors interior of $\approx 6 R_{\odot}$ are virtually identical. However, since nuclear reaction rates are sensitive to changes in temperature and density, it is these small differences that can lead to differences in the final compositions. Likewise, these small differences could lead to larger differences in the structure of the ejecta. For instance, the amount of envelope retained by the progenitor prior to core collapse could affect the growth

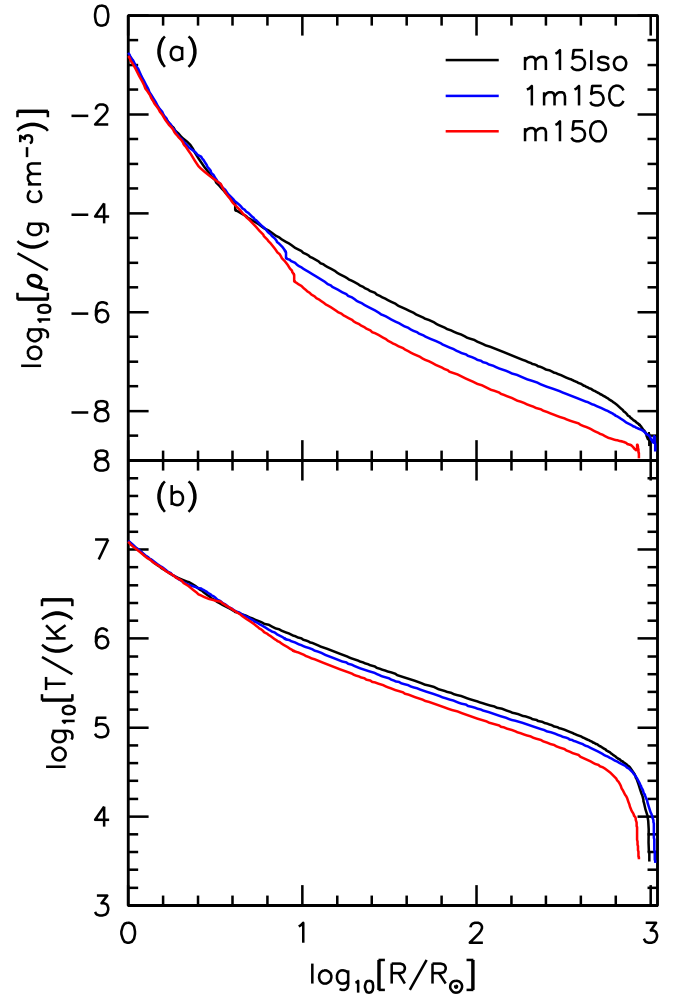


Figure 2. Top: density as a function of stellar radius for each model at the onset of core collapse. Bottom: final temperature for each model.

of instabilities during the explosion (see Wongwathanarat et al. 2015).

2.2. Supernova Models

The MESA models are coupled to a spherically symmetric (1D) Lagrangian hydrodynamics code that uses equilibrium-diffusion radiation transport. The code, called the SuperNova Explosion Code (hereafter referred to as SNEC) is made freely available and, in its publicly available form, follows the time-dependent radiation hydrodynamics and other basic physics needed for SN light-curve generation and ^{56}Ni heating. A

detailed discussion of SNEC may be found in Morozova et al. (2015), Piro & Morozova (2016), and Morozova et al. (2017).

In its basic form, SNEC couples to a model for the structure and composition of the SN progenitor. It includes the ability for an arbitrary composition and includes a prescription for mixing of ejecta, via a boxcar smoothing algorithm. Observations of SNe and remnants show both evidence for mixing of Ni-rich ejecta during the explosion (e.g., SN 1987A; Li et al. 1993) and evidence for Rayleigh–Taylor mixing between layers of differing composition and densities, and these effects are confirmed in multidimensional numerical modeling of CCSNe during the first few seconds of evolution (Janka 2012; Wongwathanarat et al. 2015, 2017). While an approximation for the Rayleigh–Taylor instability exists in one dimension (Duffell 2016), for this study we choose to ignore the mixing of metal-rich ejecta into the outer layers of the progenitor. As substantial evidence exists for the mixing of Ni and Fe-peak elements into the outer layers of ejecta, in both SNe and some SNRs, we will explore mixing in follow-up papers.

SNEC allows the user to choose between either a thermal bomb or piston-driven explosion. We choose to use the thermal bomb method, whereby we specify the core mass to be excised, and then energy is deposited in a user-specified number of mass zones, at which point the explosion calculation begins. This is a completely ad hoc method and ignores the important fact that the explosion is likely driven by a combination of neutrino heating of the shock and hydrodynamical instabilities.

Finally, SNEC closes the system of hydrodynamic conservation laws with the choice of an equation of state (EOS). The choices are either an ideal gas or the Paczynski EOS (Paczynski 1983), which includes contributions to the total pressure from radiation, ions, and electrons. While the Paczynski EOS may provide a rough approximation, it is not thermodynamically consistent, does not treat pair production, does not use a chemical potential, and is not suitable for an arbitrary composition.¹⁰ Based on these limitations, we chose instead to incorporate the Helmholtz EOS (Timmes & Swesty 2000).¹¹ The Helmholtz EOS is thermodynamically consistent. In Figure 3 we plot thermodynamic quantities and their derivatives as a function of mass coordinate in SNEC. The calculations shown in Figure 3 are for after explosive nucleosynthesis ceases. The largest differences, of order 0.5 dex, occur both at the location of the shock and in areas just above the explosion launch point. Differences between the two EOSs are most readily seen as small differences in the temperature of the shocked material, as well as differences in the pressure derivative. Nuclear burning is sensitive to the temperature, so anomalous heating due to an imprecise EOS can lead to extra burning in the ejecta. This is seen as a difference in \bar{A} in the top panel of Figure 3.

As mentioned, SNEC allows for arbitrary composition, but it does not include a way to update the composition due to explosive burning. Certainly, the additional nucleosynthesis during the explosion will not impact the observable properties of swept-up material from the CSM interaction, but it could alter the measured abundances in the ejecta. We have chosen to implement nuclear burning by using the `aprox21` network.¹² This is the same network we use in our MESA models and is an adequate yet incomplete burning network. For efficiency, we

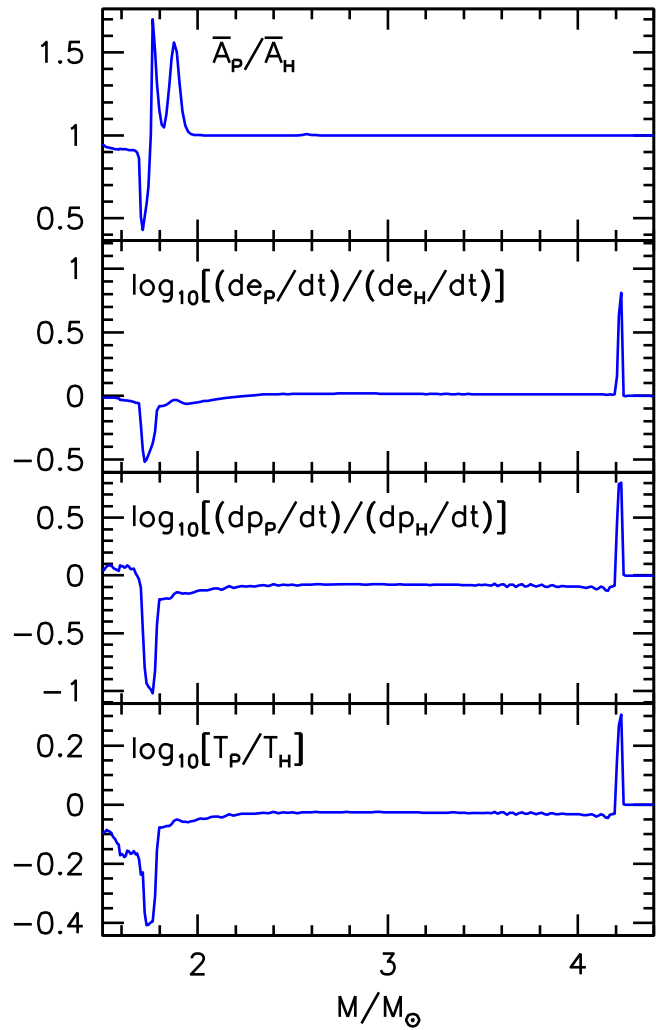


Figure 3. Differences between the Paczynski and Helmholtz EOSs. The top panel shows differences in \bar{A} (the mean atomic mass), the middle two panels show differences in the time derivatives of internal energy and pressure, and the bottom panel shows differences in the temperature.

follow the burning in each mass shell until the temperature falls below 10^7 K. As discussed in Farmer et al. (2016), the final composition is sensitive to the nuclear reaction network chosen. We defer a study of larger networks to subsequent papers.

For each pre-SN model, we assume an explosion energy of 10^{51} erg. We choose to excise the inner $1.5 M_{\odot}$ (the approximate mass of the iron core; Table 1) from the progenitor model and spread the energy across $0.1 M_{\odot}$ of ejecta, corresponding to a radial distance of ≈ 200 km above the proto-neutron star. The energy deposition lasts for 100 ms. In multidimensional studies, typical core bounce timescales are 100–200 ms (see Ott et al. 2008), so our choice of 100 ms is appropriate. The final composition and structure of the ejecta are both sensitive to the explosion energetics, but we chose values that are typical for CCSNe and consistent with 1D models of this type (Morozova et al. 2015). The explosion is followed to an age of 100 days.

We plot in Figure 4 the initial and final compositions for two of the models (m15Iso and m15O). As seen in these plots, the composition of the models both before and after core collapse are similar. In both models, as well as in model m15C, which is

¹⁰ F. X. Timmes 2017, private communication.

¹¹ http://cococubed.asu.edu/code_pages/eos.shtml

¹² http://cococubed.asu.edu/code_pages/burn.shtml

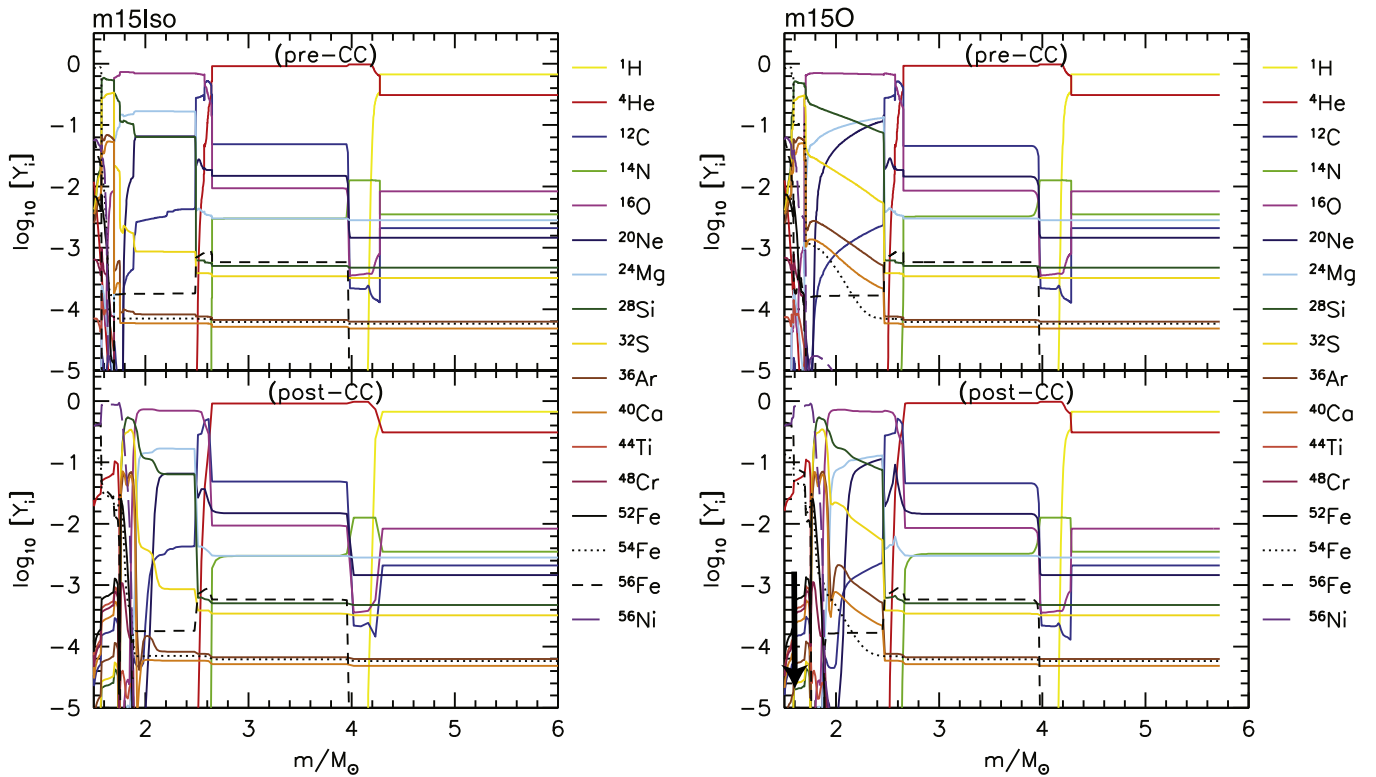


Figure 4. Left: composition profile for the $15 M_{\odot}$ model with steady mass loss (m15Iso). The top panel shows the composition of the inner $6 M_{\odot}$ prior to core collapse, while the bottom panel shows the composition for the same elements after core collapse. There is no mixing assumed in these models. Right: same as in the left panels, but for the model that underwent extreme mass loss during core oxygen burning (m15O). After evolving the models in the bottom panels for 400 yr with our ChN code, $\sim 1 M_{\odot}$ of ejecta are shocked in the isotropic wind model, while nearly all the ejecta in the highly stripped model are shocked, as indicated by the arrow in the bottom right panel.

not shown, the chemical compositions of the He-rich shell, located between mass coordinates of approximately 2.6 and $4.2 M_{\odot}$, are virtually identical, as are the compositions of the H-rich shell, exterior of $4.2 M_{\odot}$. The differences in the models are how far the H-rich shell extends. Interior of the He-rich shell, differences in composition exist in the O-rich shell between 1.8 and $2.6 M_{\odot}$, but these differences are likely due to differences that arise during the stellar evolution. Interior to this, the compositions appear identical. It is not entirely surprising that the compositions are so similar, since the same explosion conditions are applied to all three models. It is worth noting that the differences in the EOSs seen in Figure 3 correspond to locations of shell boundaries. The difference around $4.2 M_{\odot}$ corresponds to the boundary between the He- and H-rich layers, and the difference around $1.8 M_{\odot}$ corresponds to the boundary between the O-rich and Si-rich layers. Differences in the EOS calculation appear insensitive to the boundary between the O-rich and He-rich layers.

We do not report explicitly the final composition in our models (see Section 2.5). However, each model produces $\lesssim 0.2 M_{\odot}$ of ^{56}Ni and $2 \times 10^{-4} M_{\odot}$ of ^{44}Ti . Additionally, we estimate that ~ 0.5 – $0.8 M_{\odot}$ of silicon and 2 – $3 M_{\odot}$ of oxygen are in the final ejecta models.

2.3. Circumstellar Models

In general terms, the circumstellar environment is dictated by the mass loss of the progenitor and the wind velocity of the lost material. Neither parameter is completely constrained by observation (for a recent review, see Smith 2014). Velocities can vary from as little as 10 km s^{-1} in an RSG to

$\gtrsim 1000 \text{ km s}^{-1}$ in a Wolf-Rayet star. Mass-loss rates can vary from ~ 0.1 – $10 M_{\odot} \text{ yr}^{-1}$ in a luminous blue variable eruption to as low as $10^{-7} M_{\odot} \text{ yr}^{-1}$ in a helium star,¹³ and binary interactions and rotation can act to further enhance the mass loss.

As discussed in Section 2.1, we assume three mass-loss scenarios: (1) a steady wind up to core collapse; (2) the onset of a fast wind with substantial mass loss during core carbon burning, in which case this wind expands into the slower RSG wind that evolves in the CSM during hydrogen and helium burning and persists for ~ 5000 yr, and the star loses a few solar masses of material; and (3) extreme mass loss during core neon and oxygen burning, a phase that lasts for ~ 500 yr, and during which the star loses $\sim 6 M_{\odot}$ of material.

MESA does report the mass loss as a function of time, and the mass loss is observed to vary with each time step. This is entirely expected, as it is a derived quantity from other stellar parameters that are also functions of time. However, the dominant timescale in the CSM is the cooling time of swept-up shocked CSM, ~ 20 yr. This can be much longer than the relevant timescale in MESA, which is driven by the core burning and is roughly a few years during carbon burning and of order seconds during oxygen burning. In light of this, we adopt a hybrid approach.

We model the CSM as a power-law wind that is formed by the progenitor during H and He burning. This forms the CSM into which we evolve the other models and to which we compare the other models. For the isotropic wind model, we

¹³ Velocities and mass-loss rates are taken from Table 1 of Smith (2014).

adopt an average $\dot{M} \approx 5 \times 10^{-6} M_{\odot} \text{ yr}^{-1}$, with a wind speed of 15 km s^{-1} . This is the average value derived from MESA output, over the life of the star. While the main-sequence phase, which lasts for $\sim 90\%$ of the star's life, will also include some mass loss, the outer boundary of the wind-blown shell will be located at a distance of $\approx 11 \text{ pc}$ from the progenitor, assuming typical ISM parameters (see Dwarkadas 2005). Likewise, the wind from the RSG phase, which lasts $\sim 1 \text{ Myr}$, expands into this low-density bubble. During this phase, a swept-up shell forms at a distance of $\approx 3.5 \text{ pc}$. In the case of both the main sequence and RSG wind, the shell of swept-up material is at a distance that is greater than the size of the SNR at 400 yr and remains dynamically unimportant in our models.

We model the enhanced and extreme mass-loss cases in similar manners. We evolve these two cases into the steady wind produced during the earlier phases of evolution. Model m15C is evolved with a mass-loss rate of $2 \times 10^{-4} M_{\odot} \text{ yr}^{-1}$ and a velocity of 1000 km s^{-1} until the core carbon abundance is depleted below 10^{-3} . Model m15O is evolved with a mass-loss rate of $0.1 M_{\odot} \text{ yr}^{-1}$ and a velocity of order the progenitor escape velocity, $\sim 100 \text{ km s}^{-1}$. For both cases, we assume a rise time in the wind of 10 yr. For model m15C, we model the subsequent evolution after core carbon burning with a steady wind with mass-loss rates of $10^{-5} M_{\odot} \text{ yr}^{-1}$ and a wind velocity of 10 km s^{-1} . For model m15O, the extreme mass loss persists until the onset of core silicon burning, which is a short enough phase that another mass-loss model is not employed.

We use the numerical hydrodynamics code VH-1 (Blondin & Lufkin 1993) to model the evolution of the wind. VH-1 is a multidimensional general-purpose hydrodynamics code that also forms the basis of our cosmic-ray hydrodynamics code (Ellison et al. 2007). For the purposes of modeling the CSM, we have included a routine to follow radiative losses in the shocked, swept-up CSM, using both collisional and non-equilibrium ionization curves from Sutherland & Dopita (1993).

The density profiles of the modeled circumstellar environments are shown in Figure 5. While the isotropic case follows the standard $\rho_{\text{CSM}} \propto r^{-2}$, a radiatively cooled CSM shell forms in the case of the $2 \times 10^{-4} M_{\odot} \text{ yr}^{-1}$ wind. However, in the extreme mass-loss case, the shell does not cool radiatively before the simulation ends. In this case, the progenitor will explode within a few days of the exhaustion of the oxygen core. For reference, we mark the positions of the forward and reverse shocks at t_{SNR} for each model of SNR evolution, discussed in the next section.

2.4. Remnant Evolution Models

Lastly, we model the evolution of the ejecta discussed in Section 2.2 into circumstellar profiles discussed in Section 2.3. We use our cosmic-ray hydrodynamics code, hereafter called ChN to model the evolution of the ejecta to an age of $t_{\text{SNR}} = 400 \text{ yr}$. ChN is a Lagrangian hydrodynamics code that includes a prescription for diffusive shock acceleration (DSA; Ellison et al. 2007; Lee et al. 2012). We have modified the code to include the effects of DSA on non-equilibrium ionization (Patnaude et al. 2009, 2010) and have coupled the code to SN ejecta models (Lee et al. 2014; Patnaude et al. 2015). We have also included radiative losses via forbidden line cooling (Lee et al. 2015). This effect will be important in the evolution of the SN shock with a nearby CSM shell, or if we choose to model the radiative shock that could form in the ejecta during early

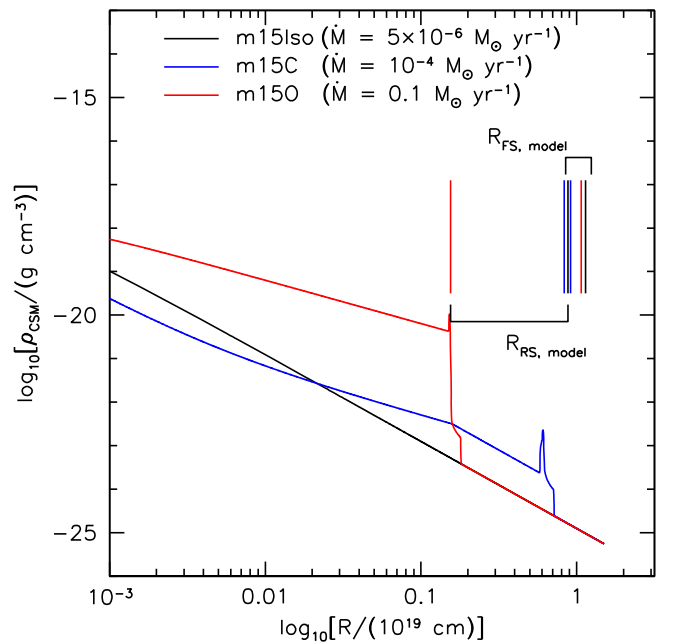


Figure 5. Circumstellar environments for each progenitor model prior to the remnant evolution. The black curve shows the CSM for model 15mISO, while the blue curve corresponds to model 15mC and the red curve to model 15mO. To accentuate the differences in the structure of the environment, we plot the base-10 logarithm of the radius. The final position of the SNR forward shock for each model is labeled. The curvature in model 15mC is the result of a ramp-down in the mass-loss rate $\approx 1000 \text{ yr}$ before the end of the simulation.

SN evolution (Nymark et al. 2006). However, we begin our simulations at an age of 5 yr, and over the lifetime of the simulation the shocks remain adiabatic, so we do not consider the radiative shock model presented in our previous work here. Since ChN couples nonlinear particle acceleration to the SNR shock dynamics, we are able to reproduce the broadband thermal and nonthermal emission (Ellison et al. 2010, 2012; Castro et al. 2012; Slane et al. 2014; Lee et al. 2013). The diffusive shock acceleration process is an integral part of ChN, and some injection of thermal particles into the acceleration process is always assumed. Here we set the injection parameter to the test particle limit, though we note that the interaction of a strong shock with a massive CSM shell or cloud will lead to enhanced particle acceleration (e.g., Ellison et al. 2012; Lee et al. 2014), and the differing ejecta profiles and compositions, may result in differences in the broadband nonthermal emission. The study of nonthermal emission in evolving SNe is sufficiently broad that we defer its study to future papers.

We simulate the SNR shock evolution to an age of 400 yr. Using the time-dependent ionization balance, we compute the thermal X-ray emission from the shocked CSM and ejecta. ChN has the capability to compute spectra from APED (Foster et al. 2012), or from a more primitive X-ray emission code discussed in Patnaude et al. (2010). While our previous studies have made use of the code discussed in Patnaude et al. (2010), we feel that the more thorough treatment provided by APED will make our simulations accessible to future high-resolution X-ray spectroscopy missions. In Figure 6, we plot the final profile of each model after 400 yr. We also plot the final average charge state for oxygen, silicon, and iron.

We plot the evolution of the synthetic X-ray spectra from each model in Figures 7 and 8. We have assumed an SNR

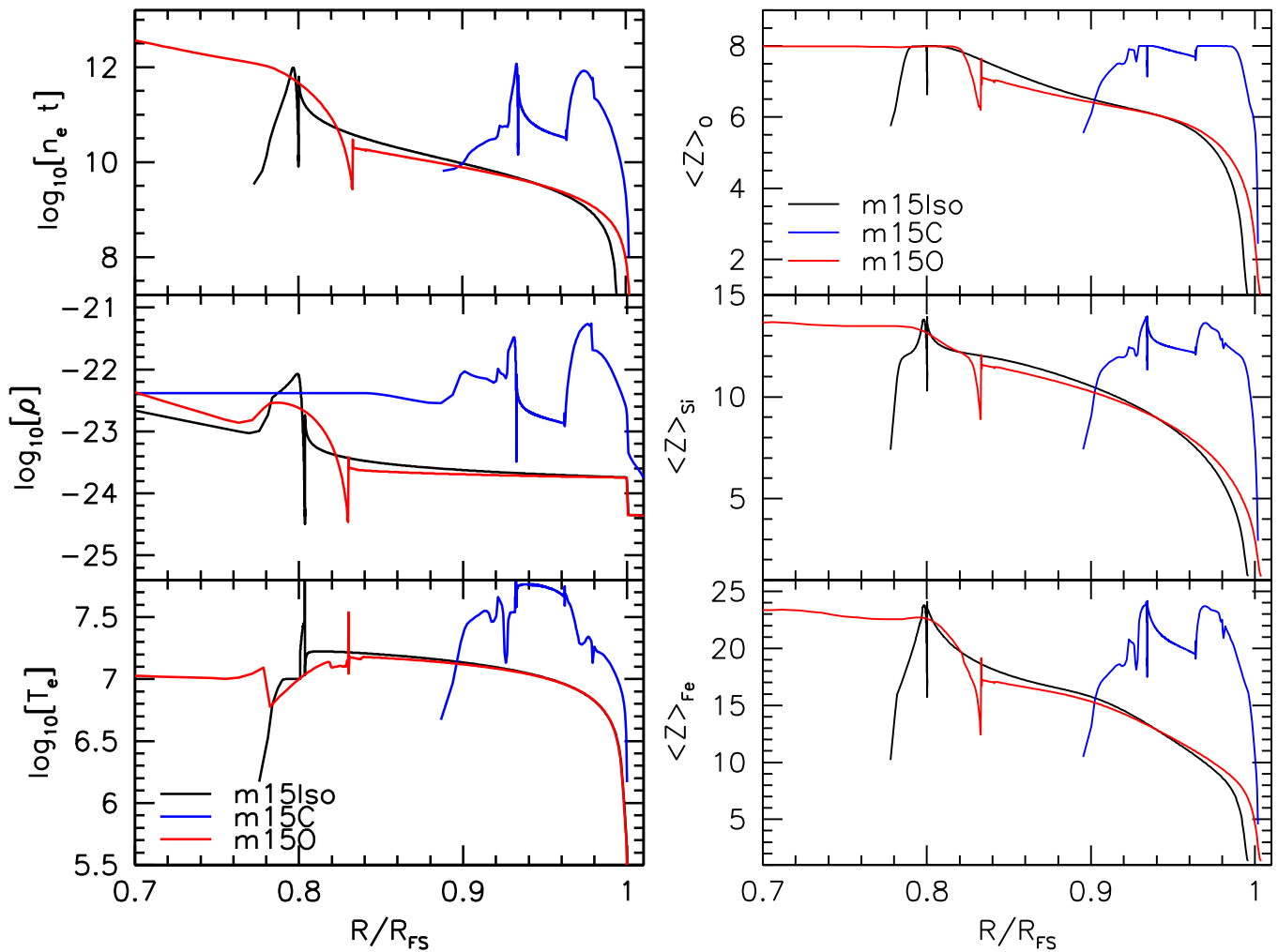


Figure 6. Left: hydrodynamical state of each model after 400 yr of evolution. The top and bottom panels show the ionization age ($n_e t$) and electron temperature (T_e) of shocked material only, while the middle panel shows the density for shocked and unshocked material. The temperature spikes seen in the plot of T_e are due to contact discontinuities in the 1D model. These spikes coincide with regions of low density and thus do not contribute to the overall emission. Right: average charge state for oxygen (top), silicon (middle), and iron (bottom).

distance of 1 kpc. The spectra have been both thermal and Doppler broadened (Lee et al. 2014), and for clarity, we do not include the effects of interstellar absorption, which can be significant below 1 keV.

2.5. Model Uncertainties

While we are not aiming to model any particular remnant in detail, each component of the model chain has uncertainty associated with both the input data and the chosen physics. Statistical uncertainties in measured nuclear and atomic cross sections are discussed in detail in their original source papers, referred to in the preceding subsections. Here we aim to understand the uncertainty that is inherent in our choice of input physics and parameters. We qualitatively summarize the uncertainty below.

For our stellar evolution models, we do not account for rotation or magnetic fields, and we choose a limited nuclear reaction network. The choice of nuclear reaction network can impact the final abundances of key elements such as oxygen and silicon in the core at core collapse by as much as 30% (Farmer et al. 2016). The exact details of the mass-loss mechanism remain poorly understood (Smith 2014). The mass-loss rates we choose, both the quasi-steady rate in the isotropic

model and the enhanced rates, span a parameter space that is broadly consistent with observed rates for steady and episodic mass loss, but given the 1D nature of our models, do not account for effects such as clumping in the wind. Additionally, we have smoothed the CSM density with a Gaussian kernel in an attempt to smear out the sharp transitions that occur around the CSM shell boundary. In reality, the transition between the power-law wind and the CSM shell may be more complicated.

In the explosion phase of our modeling, the choice of mass cut, thermal bomb duration, and bomb spread can all affect the nucleosynthesis. Young & Fryer (2007) studied variations in nucleosynthetic yields in 1D explosion models and came to the conclusion that high- Z element production is sensitive to the explosion energy and that yields may differ by as much as 50% between thermal bomb and piston-driven explosions. In essence, the yields are nonunique for a given progenitor and can vary based on how the energy is deposited in the progenitor. The progenitor masses at core collapse differ for our three models, though we choose the same explosion energy, bomb spread, and heating duration. Since the nucleosynthesis is sensitive to this and the core density and composition, and since these do not vary across the three models by much, the final abundances interior of the helium

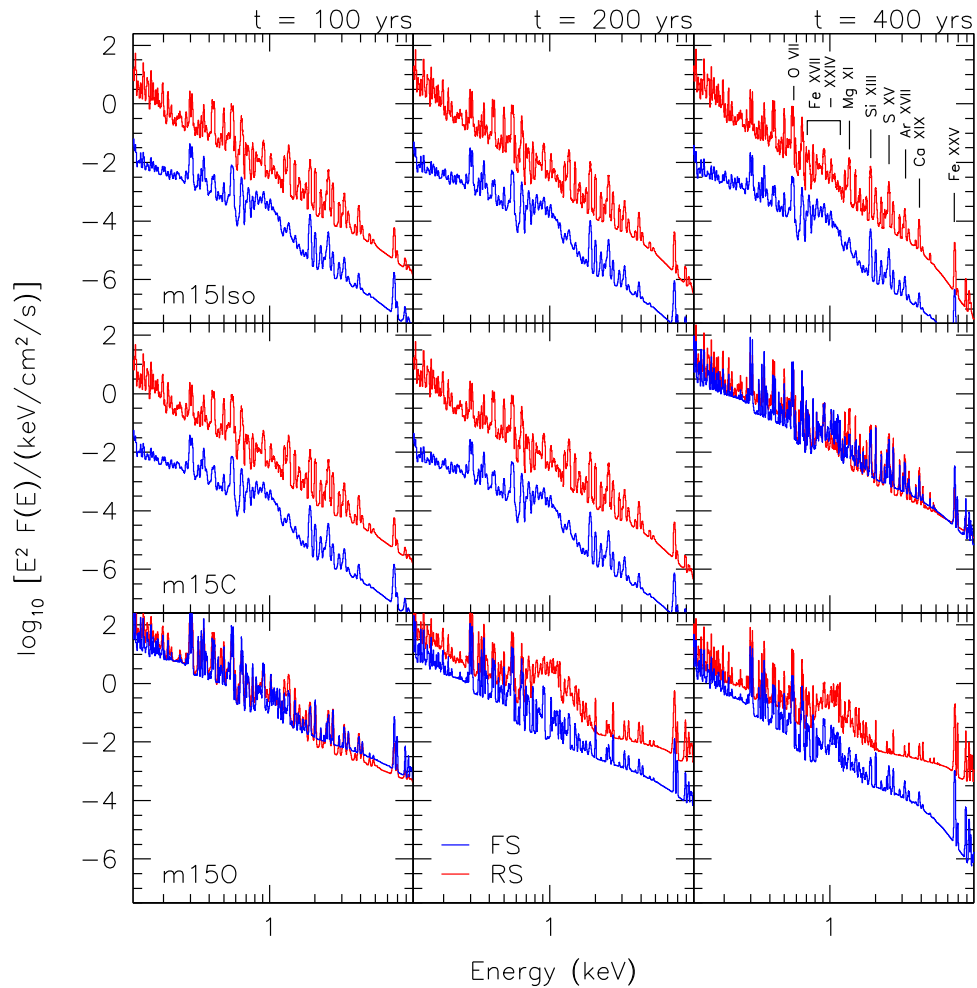


Figure 7. Simulated X-ray spectra from the forward and reverse shock for models m15Iso, m15C, and m150, at ages of 100, 200, and 400 yr. Bright He-like lines and lines from Fe XVII–Fe XXIV are marked in the top right panel.

core are very similar, with each producing $\lesssim 0.2 M_{\odot}$ of ^{56}Ni . A more dynamic reaction network would probably lower this nickel mass by quite a bit (Young & Fryer 2007), though $0.2 M_{\odot}$ of ^{56}Ni is consistent with yields expected from some CCSN models (Young & Fryer 2007). For the remnant modeling, we do not consider nonlinear shock acceleration effects, which can alter the dynamics and emitted spectrum (Ellison et al. 2007; Patnaude et al. 2011; Lee et al. 2012).

Finally, we comment on the limitations of our 1D modeling. As discussed above, we do not include the effects of rotation in the stellar evolution modeling. This can alter the mixing between layers and the treatment of convection during the stellar evolution. In the CSM, 1D models result in CSM shells, instead of a web of tenuous wind peppered by condensed clumps. For the explosion and remnant evolution modeling, 1D models are unable to follow the effects of mixing due to the Rayleigh–Taylor (RT) or Kelvin–Helmholtz instabilities. Duffell (2016) recently presented a prescription for the 1D RT instability, and we will incorporate these effects in subsequent studies. We have also not included the bulk mixing of ejecta via convective instabilities during the explosion. This will alter the abundances in the outer layers of the star, resulting in changes to the emitted X-ray spectrum from the ejecta.

Our models represent a first attempt to follow the complete evolution of a massive star from the pre-main sequence through

the remnant phase. Each phase of evolution takes as input parameters derived from a prior stage, allowing for a quasi self-consistent study of how massive star evolution affects the remnants we observe today. As is clear from the uncertainties discussed in this section, an end-to-end SN simulation requires a number of approximations and assumptions. Nevertheless, we show below that meaningful constraints on the “hidden” SN properties can be deduced from SNR observations made centuries after the explosion.

3. Modeling Results and Discussion

The principal output from ChN includes the blast-wave dynamics, as well as the broadband thermal and nonthermal emission. The results of our simulations are summarized in Table 2. For each model, we list the swept-up mass and blast-wave radius, the amount of shocked ejecta, and the bulk energy centroid for the He-like state of iron. We discuss the dynamical and spectral results below.

3.1. Model Differences

As seen in Table 2, after 400 yr, the blast-wave radii for models m15Iso and m150 are virtually identical, despite different stellar evolutionary histories. On the other hand, model m15C is $\sim 15\%$ smaller over the same time period. The

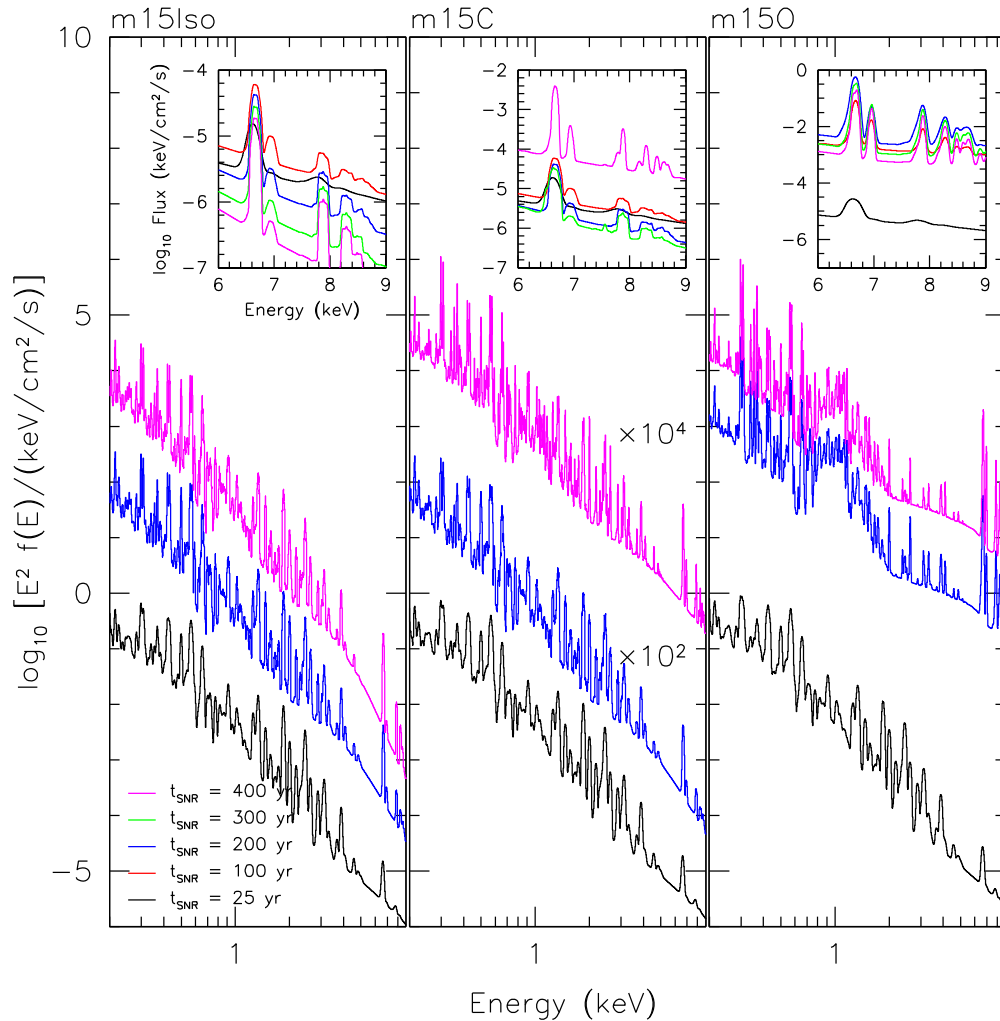


Figure 8. Integrated X-ray spectra for each model at ages between 25 and 400 yr. In the main panels we plot the spectra at ages of 25, 200, and 400 yr. The spectra at 200 and 400 yr are scaled relative to the spectra at 25 yr. The evolution of emission around Fe-K is shown in the insets and represents absolute fluxes. We plot the evolution of the Fe-K emission at 25, 100, 200, 300, and 400 yr.

Table 2
ChN Dynamical and Spectral Results at $t_{\text{SNR}} = 400$ yr

| Model | R_{FS} (pc) | M_{ej} (M_{\odot}) | $M_{\text{swept up}}$ (M_{\odot}) | He-like Fe (keV) |
|--------|-------------------------|------------------------------------|--|---------------------|
| m15Iso | 1.99 | 2.0 | 0.6 | 6.662 |
| m15C | 1.62 | 6.0 | 2.4 | 6.665 |
| m15O | 1.98 | 5.9 | 8.6 | 6.676 |

positions of the forward shock, relative to the CSM, are shown in Figure 5.

The blast-wave radii are similar for m15Iso and m15O, but the amounts of swept-up mass and shocked ejecta are remarkably different. Model m15Iso has swept up less than a solar mass of material in 400 yr and only shocked $\sim 2 M_{\odot}$ of ejecta in that time. In contrast, in m15O the blast wave has shocked $\sim 8 M_{\odot}$ of CSM material and has progressed all the way into the center of the ejecta. Model m15C represents an intermediate case, in that it has shocked about 2 and $6 M_{\odot}$ of CSM and ejecta material, respectively. Spectra from shock-heated CSM and ejecta for each model are shown in Figure 7, for ages of 100, 200, and 400 yr, and differences in the amount of shocked material are readily apparent.

As seen in Figure 7, the spectral evolutions for models m15Iso and m15C are virtually identical over the first 200 yr of their evolution. At an age of 400 yr, however, differences in their evolution become apparent, as the forward shock in model m15C interacts with the CSM shell (at $\approx t_{\text{SNR}} = 230$ yr), and emission from shocked ejecta becomes comparable to that of shocked CSM. In contrast, at 100 yr, the emission from shocked ejecta and that from shocked CSM are comparable in model m15O. In this model, the shock interacts with the CSM shell at ≈ 40 yr and breaks out ≈ 100 yr later. By 200 yr, the forward shock is well into the lower-density pre-shell wind, so the emission from swept-up CSM begins to drop, due to adiabatic expansion.

As listed in Table 2, both models m15C and m15O have swept over a comparable amount of ejecta. However, the composition of the shocked ejecta is quite different. At the time of core collapse, model m15C still has an H-rich envelope of mass $\sim 8 M_{\odot}$. The H-rich envelope for model m15O is only $\approx 2 M_{\odot}$. Additionally, as seen in Figure 2, exterior of $R \approx 10 R_{\odot}$, the density of model m15O is lower than that of either m15C or m15Iso. Not only is the progenitor of m15O more compact than the other models, but it also has a lower-density envelope—the reverse shock can travel all the way into the center of the ejecta after only 400 yr. At 400 yr, model

m150 has already transitioned to the Sedov phase. This rapid transition is likely aided by the dense CSM shell.

In Figure 8 we plot the time evolution of the total thermal X-ray spectrum at $t_{\text{SNR}} = 25, 200,$ and 400 yr. For each model, we offset the spectrum from each epoch, for ease of comparison. We also show, in the inset, the evolution of the spectrum from 6 to 7 keV, without an offset. Even with the offset in the y-axis, the changes in the spectrum as the SNR evolves are apparent between the three models. In model m150, a sharp increase in Fe-L shell (Fe XVII–Fe XXIV) emission around 1 keV is seen after 200 yr, while by 400 yr much of the Fe emission comes from K-shell emission. In contrast, as expected, there is a dramatic rise in the total X-ray emission in model m150 between 25 and 200 yr. Even after the shock breaks out of the shell, Fe-L shell emission and K-shell emission continue to increase over the remainder of the SNR’s evolution, probably as the reverse shock probes the deeper layers of the ejecta. This is best exemplified when contrasting the bottom row of Figure 7 with the right column of Figure 8: the X-ray emission from reverse-shock-heated material (red curves of Figure 7) rises between 100 and 200 yr and only declines a bit over the next 200 yr. In contrast, emission from shocked CSM drops steadily across the three epochs in these two models. The late-time Fe emission shown in Figure 8 from model m150 arises predominantly from shocked ejecta.

We plot the absolute line fluxes for K-shell emission in the inset panels of Figure 8 and list the centroid energies at $t_{\text{SNR}} = 400$ yr in Table 2. Model m150 results in a considerably higher line centroid at 400 yr than the other two models (~ 10 eV greater). As seen in the inset, the absolute line fluxes are nearly 2 orders of magnitude higher as well. This is expected: the blast wave has both swept up more material in the CSM and shocked more ejecta than the other models. The overall emission measure for model m150 is higher, producing a higher overall flux, and the ionization timescale $\tau = \int n_e(t) dt$ is much larger as well, resulting in a higher ionization state (see Figure 6).

Finally, in Figures 9 and 10, we plot the line-of-sight-integrated spectra for three fiducial radii and the projected 6.4–6.8 keV emissivity. We include both Doppler and thermal broadening in the spectral computations. At an age of 400 yr, Doppler shifts are still detected toward the center of the SNR, allowing for discrimination between blueshifted and redshifted ejecta out to radii of $0.75R_{\text{FS}}$. We highlight emission around Si XIII. As seen in Figure 9, there does not appear to be any emission from this state of silicon in models m15Iso and m150 at a radius of $0.95R_{\text{FS}}$. This is confirmed by the low charge state of silicon near the forward shock in these models, seen in the middle right panel of Figure 6, and in contrast to the much higher average charge state of silicon in model m15C.

For the line-of-sight Fe-K emission, models m15Iso and m150 show expected profiles. Interior to the contact interface, the Fe-K emission is dominated by emission from the reverse shock. Exterior to this, emission is from the shocked CSM only. In the case of model m15C, emission is primarily from forward-shocked material everywhere. This is likely due to the strong interaction between the blast wave and the CSM shell. Interestingly, the reverse-shock-heated material is projected nearly to the forward shock. This is due to the fact that the forward shock is strongly decelerated in the shell. The radius of the contact interface in our model is $0.93R_{\text{FS}}$. For Figure 10, we choose extraction regions with resolution $0.1R_{\text{FS}}$. While the

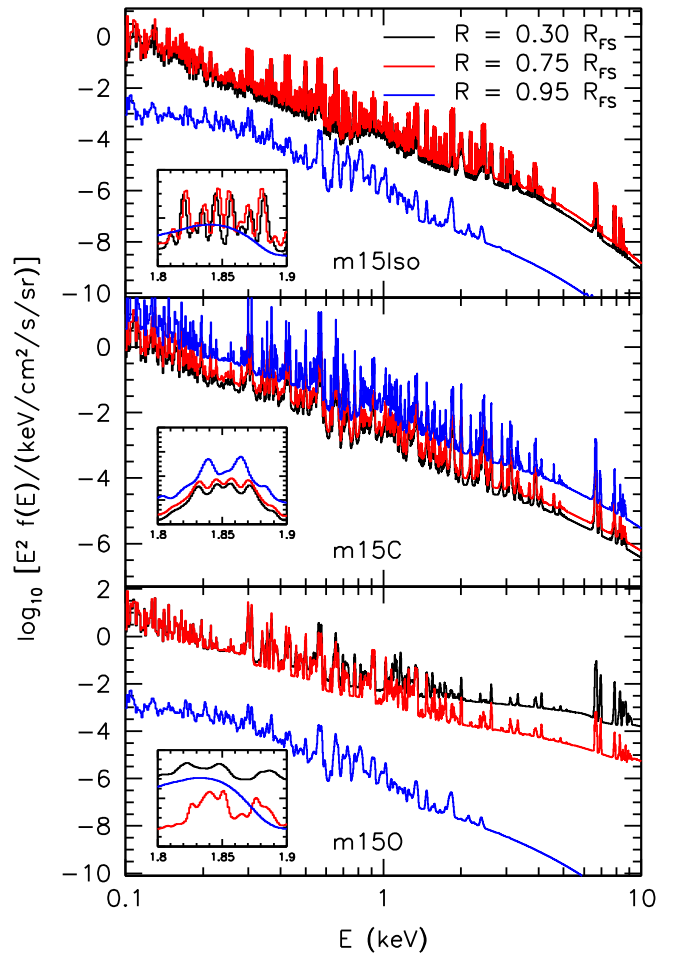


Figure 9. Integrated spectra for models m15Iso (top), m15C (middle), and m150 (bottom), for projected radii of $0.3R_{\text{FS}}$, $0.75R_{\text{FS}}$, and $0.95R_{\text{FS}}$. Each radial extraction is of width $dR/R_{\text{FS}} = 0.1$. The inset regions show the line emission centered around Si XIII. For ease of comparison, the line profiles have been scaled by an arbitrary amount. The Doppler shifting of the line emission is seen most readily in models m15Iso and m15C. The redshifted lines have not been corrected for absorption.

contact interface is very close to the forward shock, our choice of extraction bin size results in the outermost bin of shocked ejecta being projected to the radius of the forward shock.

3.2. Implications for Progenitor Identification

In the absence of a light echo spectrum that can be compared to template spectra for CCSNe, relating a remnant back to its progenitor evolution remains tricky. As already discussed here, important mass-loss processes can be triggered by several channels, including binary interaction and enhanced or episodic mass loss. Additionally, the once clear road map between progenitor and SN type is more muddled, as SNe are now observed to migrate between types as they evolve (e.g., Milisavljevic et al. 2015).

In specific terms, there have been several attempts to connect SNRs back to their progenitors. Most recently, Katsuda et al. (2015) detected thermal X-ray emission from the synchrotron-dominated SNR RX J1713.7–3946. They found that the measured abundances favored a low-mass progenitor, and that it likely lost much of its mass through binary interaction. This is at odds with previous work that considered a massive O star

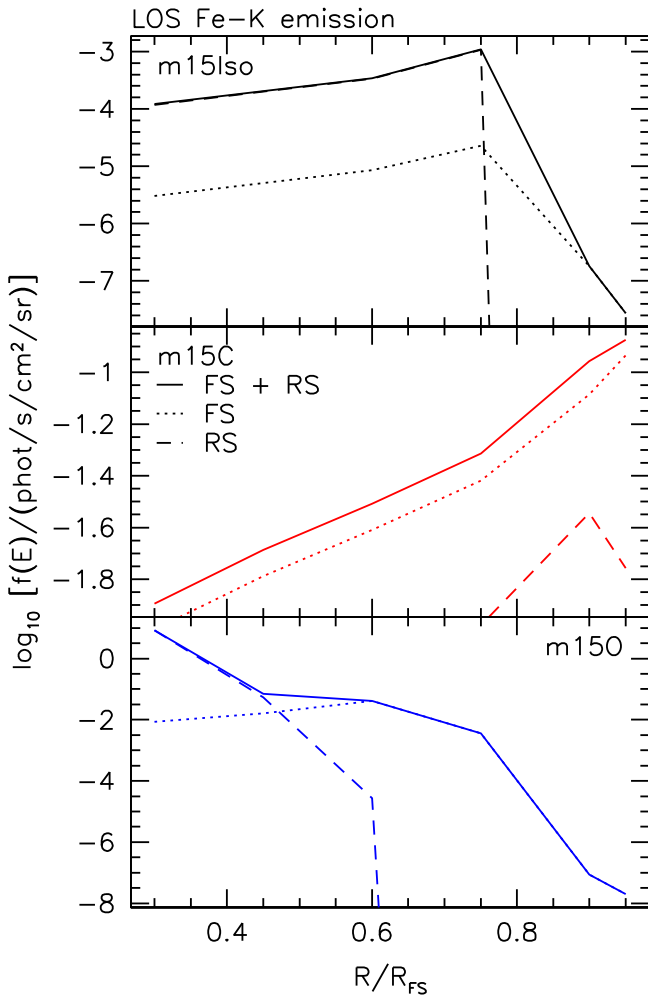


Figure 10. Line-of-sight-projected emission from 6.4 to 6.8 keV, highlighting emission from helium-like iron. The top panel corresponds to model *m15Iso*, the middle panel to *m15C*, and the bottom panel to *m150*. Each panel shows the contribution to the total flux from both the forward and reverse shocks. In the case of model *m15C*, the shocked ejecta have caught up to the shocked CSM, as the forward shock moves through the CSM shell, over a radial distance that is unresolved by the choice of radial binning. All the plots have been normalized to the forward shock radii for each model.

that carved out a large wind-blown bubble that the progenitor proceeded to explode into (e.g., Ellison et al. 2012).

More generally, Chevalier (2005) looked at the morphologies of several Galactic SNRs, combined with qualities of their central compact objects, and typed several as IIPs, IILs, or IIbs, dependent on the amount of mass estimated to have been lost during stellar evolution.

ChN has the capability to compute X-ray light curves. Dwarkadas & Gruszko (2012) compiled the light curves for all known X-ray SNe and showed that many deviate from the expected $L_X \propto t^{-1}$ behavior. In Figure 11, we plot the 0.5–10 keV light curves for the three models. The light curves are distance and absorption independent.

As seen in Figure 11, there is a steady decline in the X-ray emission in model *m15Iso*, while the models with non-steady mass loss show different behavior—model *m150* shows a sharp increase in luminosity due to the early interaction between the blast wave and CSM shell, while model *m15C* follows model *m15Iso* closely before the shock-shell interaction. We have overlaid the current X-ray luminosity

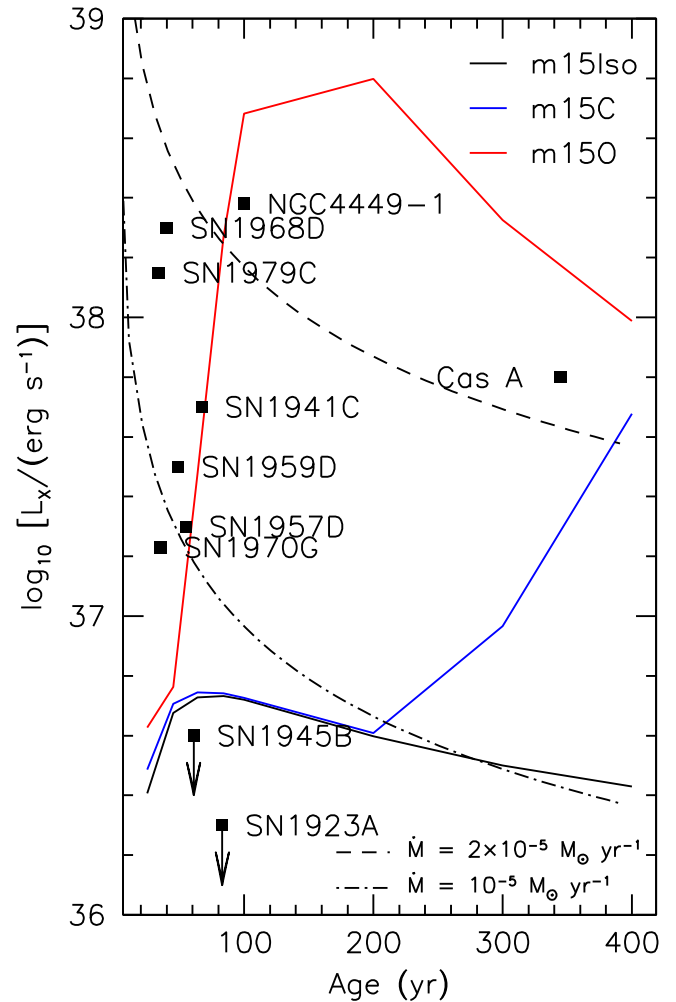


Figure 11. The 0.5–10.0 keV X-ray luminosity for each model. Also shown are the approximate X-ray luminosities for several historical SNRs, as well as the expected X-ray luminosity due to free-free emission for mass-loss rates of 10^{-5} and $2 \times 10^{-5} M_{\odot} \text{ yr}^{-1}$, assuming isotropic mass loss (Immler & Lewin 2003). Data are taken from Patnaude & Fesen (2003), Stockdale et al. (2006), Soria & Perna (2008), Patnaude et al. (2011), Long et al. (2012), and Ross & Dwarkadas (2017).

for select historical CCSNe, as well as theoretical curves for the X-ray emission as a function of time for a range of mass-loss rates and wind velocities (Immler & Lewin 2003). While we are not aiming to model any particular SNR, it is worth noting that the data from any particular SNR are inconsistent with neither the luminosity predictions from our models nor the predictions from self-similar models such as those shown in Figure 11.

Dwarkadas & Gruszko (2012) published historical light curves for 41 X-ray SNe. They showed that the light curves do not decline as t^{-1} as would be expected from isotropic mass loss. They argued that some of this is due to how the X-ray temperature changes as the blast wave evolves, resulting in differing *observed* emission as the peak of the emissivity function changes, but some of the trends they observe in the light curves may also be due to the structure of the circumstellar environment. The theoretical curves presented in Figure 11 represent contributions from shocked CSM only and do not account for the delayed rise in X-ray emission from shocked ejecta (see right panel of Figure 1 of Patnaude et al. 2015). Qualitatively, the luminosities in the isotropic mass-loss

models are similar to those in our models, but they assume a steady decline in the CSM density, which is clearly not the case for our models m_{15C} and m_{15O} . Of additional interest are the large differences in luminosity between observations and our models (and the self-similar models overplotted in Figure 11). As seen in Dwarkadas & Gruszko (2012), the X-ray luminosity for several of their SNe varies between 10^{38} and 10^{40} erg s^{-1} over the first few decades of SN evolution. These observed luminosities are much higher than what we see in our models at early epochs. We interpret this as meaning that the mass-loss rates are $>10^{-5} M_{\odot} \text{ yr}^{-1}$ prior to core collapse, or that dense CSM shells exist at radii $<10^{17}$ cm. Observations of recent and not-so-recent SNe support this (e.g., SN 1996cr, SN 2005kd, and SN 2014C; Dwarkadas et al. 2010, 2016; Margutti et al. 2017). Alternatively, the models presented here begin at an age of 5 yr after core collapse. Choosing a starting age for our simulation closer to the time of core collapse would likely result in higher X-ray luminosities earlier in the evolution, in line with the self-similar predictions.

An interesting feature of Figure 11 is the gap of observational data between ~ 50 and 100 yr old extragalactic remnants and the ~ 340 yr old Cas A SNR. Remnants with ages of ~ 100 yr probe the mass-loss history in the latter stages of the RSG phase, an interesting time in massive-star evolution. Future X-ray observatories such as *Athena* will be able to access these epochs in young SNRs such as SN 1957D and NGC 4449-1.

When comparing the X-ray light curves in Figure 11, it becomes clear that the integrated X-ray emission from an SN or SNR does not tell the full story. At any one epoch, dissimilar mass-loss rates can give similar L_X values. Examining the dynamics and the detailed ionization state of the gas will break the degeneracy. For instance, at ages of 400 yr, model m_{15C} and the self-similar model with a steady $2 \times 10^{-5} M_{\odot} \text{ yr}^{-1}$ differ in luminosity by less than 0.1 dex. At that age, m_{15C} has a radius of 1.62 pc. In contrast, the blast-wave radius for a 400 yr old SNR with constant mass loss is ~ 4 pc (see right panel of Figure 1 of Patnaude et al. 2015). From Patnaude et al. (2015), the Fe-K luminosity for a model with a mass-loss rate of $2 \times 10^{-5} M_{\odot} \text{ yr}^{-1}$ is estimated to be $\lesssim 10^{42}$ photons s^{-1} . The luminosity in the Fe-K line in model m_{15C} is estimated to be $\gtrsim 400\times$ this. Even though the broadband X-ray luminosities between the models are quite close, the details of the dynamics and ionization balance of the shocked material tell a different story about how the blast wave interacted with the pre-SN environment.

4. Conclusions

We have presented the first quasi-self-consistent models for the evolution of $15 M_{\odot}$ stars from the pre-main sequence through core collapse and into the remnant phase. To our knowledge, this is the first attempt to produce such an end-to-end simulation in a self-consistent fashion. We have followed the evolution of the remnant to an age of 400 yr, at which point one of our models, m_{15O} , has entered the Sedov phase. The only difference between the three models is the mass-loss history of the progenitor. We find that the mass loss in late stages (during and after core carbon burning) can have a profound impact on the dynamics and spectral evolution of the SNR. While our models are currently not tailored to any particular SN or SNR, we note the following:

1. Extreme mass loss during core neon or oxygen burning can result in CSM shells at distances >0.5 pc. While the shell is not in the immediate vicinity of the progenitor, the shock/shell interaction will leave its imprint on the emitted X-ray spectrum centuries after the shock has broken through the shell.
2. Enhanced mass loss during post core helium burning phases can result in CSM shells at radii of less than a couple of parsecs. These shells are created only a few thousand years prior to core collapse. While we do expect them to collapse to thin shells as a result of radiative cooling, the shell will persist through progenitor core collapse. Depending on the energetics, the blast wave will interact with the remnant of the shell up to a couple of hundred years after core collapse, resulting in an increase in X-ray emission from the shocked CSM. Our 1D models, which do not follow in detail the dynamical and radiative evolution of the shell after its formation, which may lead to clumping or fragmentation of the shell, provide an upper limit on the amount of X-ray emission from the shock-shell interaction in this scenario.
3. In Patnaude et al. (2015), we postulated that enhanced mass loss in the years leading up to core collapse would result in increased X-ray emission, with little impact on the late-time dynamics. Our simulations bear this out—CSM shells close to the progenitor result in a sharp increase in the X-ray emission up to a century after core collapse. However, once the shock breaks through the shell, it accelerates and the forward shock is dynamically similar to models with isotropic mass loss. We expect that this is due to the energetics of the explosion: in models with enhanced or extreme mass loss, the specific energy of the ejecta is higher than in the more massive model (by about a factor of 2). During the early phases of the remnant evolution, the blast-wave dynamics are not strongly determined by the CSM structure, since the total mass in the ejecta is half that of the isotropic mass-loss model. This argues that when considering the X-ray emission from SNRs, the mass-loss history of the progenitor should be carefully considered. *Where* and *when* the mass was deposited in the CSM can have a profound impact on the evolution of the remnant.

Our models are not yet tailored to pinpoint the evolutionary history of any one SNR. However, given the high-fidelity data that currently exist for both evolved ($t_{\text{SNR}} \sim 1000$ yr) and young ($t_{\text{SNR}} \lesssim 100$ yr) SNRs, the progenitor mass-loss history can be reconstructed with reasonable precision (see, e.g., Dwarkadas & Gruszko 2012). Thus, Galactic and extragalactic SNRs may now (or in the future) be probed as a class of objects. With the forthcoming advent of high spatial and spectral resolution microcalorimeters on missions such as *Athena* and *Lynx*, we can probe the progenitor evolution of extragalactic SNe and SNRs by studying the detailed evolution of their spectra and comparing them to our evolutionary models.

The authors thank Frank Timmes, H. Thomas Janka, Randall Smith, and Rob Fesen for fruitful discussions. Additionally, we are grateful to Mathieu Renzo for useful comments during the preparation of this manuscript, as well as to the anonymous referee. D.J.P. acknowledges support from the *Chandra* Theory Program NASA/TM6-17003X and NASA contract NAS8-03060.

Software: MESA (Paxton et al. 2011, 2013, 2015), SNEC (Morozova et al. 2015), VH-1 (Blondin & Lufkin 1993), APED (Foster et al. 2012).

ORCID iDs

Daniel J. Patnaude  <https://orcid.org/0000-0002-7507-8115>
 Patrick O. Slane  <https://orcid.org/0000-0002-6986-6756>
 Carles Badenes  <https://orcid.org/0000-0003-3494-343X>
 Shigehiro Nagataki  <https://orcid.org/0000-0002-7025-284X>
 Donald C. Ellison  <https://orcid.org/0000-0003-0037-2288>
 Dan Milisavljevic  <https://orcid.org/0000-0002-0763-3885>

References

- Blondin, J. M., & Lufkin, E. A. 1993, *ApJS*, 88, 589
 Castro, D., Slane, P., Ellison, D. C., & Patnaude, D. J. 2012, *ApJ*, 756, 88
 Chakraborti, S., Ray, A., Smith, R., et al. 2016, *ApJ*, 817, 22
 Chevalier, R. A. 2005, *ApJ*, 619, 839
 Chugai, N. N., & Chevalier, R. A. 2006, *ApJ*, 641, 1051
 de Mink, S. E., Langer, N., Izzard, R. G., Sana, H., & de Koter, A. 2013, *ApJ*, 764, 166
 Duffell, P. C. 2016, *ApJ*, 821, 76
 Dwarkadas, V. V. 2005, *ApJ*, 630, 892
 Dwarkadas, V. V. 2007, *ApJ*, 667, 226
 Dwarkadas, V. V., Dewey, D., & Bauer, F. 2010, *MNRAS*, 407, 812
 Dwarkadas, V. V., & Gruszko, J. 2012, *MNRAS*, 419, 1515
 Dwarkadas, V. V., Romero-Cañizales, C., Reddy, R., & Bauer, F. E. 2016, *MNRAS*, 462, 1101
 Elias-Rosa, N., Pastorello, A., Benetti, S., et al. 2016, *MNRAS*, 463, 3894
 Ellison, D. C., Patnaude, D. J., Slane, P., Blasi, P., & Gabici, S. 2007, *ApJ*, 661, 879
 Ellison, D. C., Patnaude, D. J., Slane, P., & Raymond, J. 2010, *ApJ*, 712, 287
 Ellison, D. C., Slane, P., Patnaude, D. J., & Bykov, A. M. 2012, *ApJ*, 744, 39
 Farmer, R., Fields, C. E., Petermann, I., et al. 2016, *ApJS*, 227, 22
 Foster, A. R., Ji, L., Smith, R. K., & Brickhouse, N. S. 2012, *ApJ*, 756, 128
 Fraser, M., Inserra, C., Jerkstrand, A., et al. 2013, *MNRAS*, 433, 1312
 Glebbeek, E., Gaburov, E., de Mink, S. E., Pols, O. R., & Portegies Zwart, S. F. 2009, *A&A*, 497, 255
 Immler, S., & Lewin, W. H. G. 2003, in *Supernovae and Gamma-Ray Bursters, Lecture Notes in Physics*, Vol. 598, ed. K. Weiler (Berlin; Heidelberg: Springer-Verlag), 91
 Janka, H.-T. 2012, *ARNPS*, 62, 407
 Kamble, A., Margutti, R., Soderberg, A. M., et al. 2016, *ApJ*, 818, 111
 Katsuda, S., Acero, F., Tominaga, N., et al. 2015, *ApJ*, 814, 29
 Kuncarayakti, H., Maeda, K., Anderson, J. P., et al. 2016, *MNRAS*, 458, 2063
 Lee, J.-J., Park, S., Hughes, J. P., et al. 2010, *ApJ*, 711, 861
 Lee, S.-H., Ellison, D. C., & Nagataki, S. 2012, *ApJ*, 750, 156
 Lee, S.-H., Patnaude, D. J., Ellison, D. C., Nagataki, S., & Slane, P. O. 2014, *ApJ*, 791, 97
 Lee, S.-H., Patnaude, D. J., Raymond, J. C., et al. 2015, *ApJ*, 806, 71
 Lee, S.-H., Slane, P. O., Ellison, D. C., Nagataki, S., & Patnaude, D. J. 2013, *ApJ*, 767, 20
 Li, H., McCray, R., & Sunyaev, R. A. 1993, *ApJ*, 419, 824
 Long, K. S., Blair, W. P., Godfrey, L. E. H., et al. 2012, *ApJ*, 756, 18
 Maeda, K., Hattori, T., Milisavljevic, D., et al. 2015, *ApJ*, 807, 35
 Margutti, R., Kamble, A., Milisavljevic, D., et al. 2017, *ApJ*, 835, 140
 Margutti, R., Milisavljevic, D., Soderberg, A. M., et al. 2014, *ApJ*, 780, 21
 Mauerhan, J. C., Smith, N., Filippenko, A. V., et al. 2013, *MNRAS*, 430, 1801
 Milisavljevic, D., Margutti, R., Kamble, A., et al. 2015, *ApJ*, 815, 120
 Milisavljevic, D., Margutti, R., Soderberg, A. M., et al. 2013, *ApJ*, 767, 71
 Morozova, V., Piro, A. L., Renzo, M., et al. 2015, *ApJ*, 814, 63
 Morozova, V., Piro, A. L., & Valenti, S. 2017, *ApJ*, 838, 28
 Nieuwenhuijzen, H., & de Jager, C. 1990, *A&A*, 231, 134
 Nugis, T., & Lamers, H. J. G. L. M. 2000, *A&A*, 360, 227
 Nymark, T. K., Fransson, C., & Kozma, C. 2006, *A&A*, 449, 171
 Ofek, E. O., Sullivan, M., Cenko, S. B., et al. 2013, *Natur*, 494, 65
 Ofek, E. O., Sullivan, M., Shaviv, N. J., et al. 2014, *ApJ*, 789, 104
 Ott, C. D., Burrows, A., Dessart, L., & Livne, E. 2008, *ApJ*, 685, 1069
 Paczynski, B. 1983, *ApJ*, 267, 315
 Pastorello, A., Cappellaro, E., Inserra, C., et al. 2013, *ApJ*, 767, 1
 Pastorello, A., Mattila, S., Zampieri, L., et al. 2008, *MNRAS*, 389, 113
 Patnaude, D., & Badenes, C. 2017, arXiv:1702.03228
 Patnaude, D. J., Ellison, D. C., & Slane, P. 2009, *ApJ*, 696, 1956
 Patnaude, D. J., & Fesen, R. A. 2003, *ApJ*, 587, 221
 Patnaude, D. J., Lee, S.-H., Slane, P. O., et al. 2015, *ApJ*, 803, 101
 Patnaude, D. J., Loeb, A., & Jones, C. 2011, *NewA*, 16, 187
 Patnaude, D. J., Slane, P., Raymond, J. C., & Ellison, D. C. 2010, *ApJ*, 725, 1476
 Paxton, B., Bildsten, L., Dotter, A., et al. 2011, *ApJS*, 192, 3
 Paxton, B., Cantiello, M., Arras, P., et al. 2013, *ApJS*, 208, 4
 Paxton, B., Marchant, P., Schwab, J., et al. 2015, *ApJS*, 220, 15
 Piro, A. L., & Morozova, V. S. 2016, *ApJ*, 826, 96
 Podsiadlowski, P., Joss, P. C., & Hsu, J. J. L. 1992, *ApJ*, 391, 246
 Quataert, E., & Shiode, J. 2012, *MNRAS*, 423, L92
 Ross, M., & Dwarkadas, V. V. 2017, *AJ*, 153, 246
 Shiode, J. H., & Quataert, E. 2014, *ApJ*, 780, 96
 Slane, P., Lee, S.-H., Ellison, D. C., et al. 2014, *ApJ*, 783, 33
 Smith, N. 2014, *ARA&A*, 52, 487
 Smith, N., & Arnett, W. D. 2014, *ApJ*, 785, 82
 Smith, N., Kilpatrick, C. D., Mauerhan, J. C., et al. 2017, *MNRAS*, 466, 3021
 Smith, N., Mauerhan, J. C., & Prieto, J. L. 2014, *MNRAS*, 438, 1191
 Soria, R., & Perna, R. 2008, *ApJ*, 683, 767
 Stockdale, C. J., Maddox, L. A., Cowan, J. J., et al. 2006, *AJ*, 131, 889
 Sutherland, R. S., & Dopita, M. A. 1993, *ApJS*, 88, 253
 Timmes, F. X., & Swesty, F. D. 2000, *ApJS*, 126, 501
 Truelove, J. K., & McKee, C. F. 1999, *ApJS*, 120, 299
 Vink, J. S., de Koter, A., & Lamers, H. J. G. L. M. 2001, *A&A*, 369, 574
 Wongwathanarat, A., Janka, H.-T., Müller, E., Pllumbi, E., & Wanajo, S. 2017, *ApJ*, 842, 13
 Wongwathanarat, A., Müller, E., & Janka, H.-T. 2015, *A&A*, 577, A48
 Yoon, S.-C., & Cantiello, M. 2010, *ApJL*, 717, L62
 Young, P. A., & Fryer, C. L. 2007, *ApJ*, 664, 1033